


Enhanced extreme ultraviolet high-harmonic generation from chromium-doped magnesium oxide

Cite as: Appl. Phys. Lett. **118**, 201103 (2021); <https://doi.org/10.1063/5.0047421>

Submitted: 13 February 2021 . Accepted: 13 April 2021 . Published Online: 17 May 2021

V. E. Nefedova, S. Fröhlich,  F. Navarrete,  N. Tancogne-Dejean, D. Franz, A. Hamdou, S. Kaassamani, D. Gauthier,  R. Nicolas, G. Jargot,  M. Hanna, P. Georges,  M. F. Ciappina,  U. Thumm,  W. Boutu, and  H. Merdji

COLLECTIONS

 This paper was selected as Featured



View Online



Export Citation



CrossMark

ARTICLES YOU MAY BE INTERESTED IN

Ultrawide bandgap semiconductors

Applied Physics Letters **118**, 200401 (2021); <https://doi.org/10.1063/5.0055292>

Effect of dipolar interaction on exceptional points in synthetic layered magnets

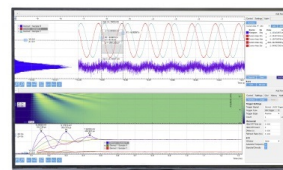
Applied Physics Letters **118**, 202401 (2021); <https://doi.org/10.1063/5.0049011>

Electric-field effect on magnetic moments in Co ultra-thin films deposited on Pt

Applied Physics Letters **118**, 152405 (2021); <https://doi.org/10.1063/5.0049052>

Challenge us.

What are your needs for periodic signal detection?



Zurich Instruments

Enhanced extreme ultraviolet high-harmonic generation from chromium-doped magnesium oxide

Cite as: Appl. Phys. Lett. **118**, 201103 (2021); doi: 10.1063/5.0047421

Submitted: 13 February 2021 · Accepted: 13 April 2021 ·

Published Online: 17 May 2021



View Online



Export Citation



CrossMark

V. E. Nefedova,¹ S. Fröhlich,¹ F. Navarrete,^{2,3}  N. Tancogne-Dejean,⁴  D. Franz,¹ A. Hamdou,¹ S. Kaassamani,¹ D. Gauthier,¹ R. Nicolas,^{1,5}  G. Jargot,^{6,7} M. Hanna,⁶  P. Georges,⁶ M. F. Ciappina,^{8,9,10}  U. Thumm,^{2,a)}  W. Boutu,¹  and H. Merdji^{1,a)} 

AFFILIATIONS

¹Ultrafast Nanophotonics Group, LIDYL, CEA-CNRS-Université Paris-Saclay, 91191 Gif-sur-Yvette, France

²Department of Physics, Kansas State University, Manhattan, Kansas 66506, USA

³Institute of Physics, University of Rostock, 18051 Rostock, Germany

⁴Max Planck Institute for the Structure and Dynamics of Matter and Center for Free-Electron Laser Science, Luruper Chaussee 149, 22761 Hamburg, Germany

⁵Department of Natural Sciences, Lebanese American University, 1102 Beirut, Lebanon

⁶Université Paris-Saclay, Institut d'Optique Graduate School, CNRS, Laboratoire Charles Fabry, 91127 Palaiseau, France

⁷Fastlite, Sophia Antipolis, 06600 Antibes, France

⁸ICFO-Institut de Ciències Fòniques, The Barcelona Institute of Science and Technology, Avenue Carl Friedrich Gauss 3, 08860 Castelldefels (Barcelona), Spain

⁹Physics Program, Guangdong Technion-Israel Institute of Technology, Shantou, Guangdong 515063, China

¹⁰Technion-Israel Institute of Technology, Haifa 32000, Israel

^{a)}Authors to whom correspondence should be addressed: thumm@phys.ksu.edu and hamed.merdji@cea.fr

ABSTRACT

High-order harmonic generation (HHG) from crystals is emerging as a new ultrashort source of coherent extreme ultraviolet (XUV) light. Doping the crystal structure can offer a new way to control the source properties. Here, we present a study of HHG enhancement in the XUV spectral region from an ionic crystal, using dopant-induced vacancy defects, driven by a laser centered at a wavelength of 1.55 μm . Our numerical simulations based on solutions of the semiconductor Bloch equations and density-functional theory are supported by our experimental observations and demonstrate an increase in the XUV high harmonic yield from doped bulk magnesium oxide (MgO) compared to undoped MgO, even at a low defect concentration. The anisotropy of the harmonic emission as a function of the laser polarization shows that the pristine crystal's symmetry is preserved. Our study paves the way toward the control of HHG in solids with complex defects caused by transition-metal doping.

© 2021 Author(s). All article content, except where otherwise noted, is licensed under a Creative Commons Attribution (CC BY) license (<http://creativecommons.org/licenses/by/4.0/>). <https://doi.org/10.1063/5.0047421>

The interaction of an electric field in the strong-field regime with a semiconductor or a dielectric generates electron-hole pairs, which are subsequently accelerated by this field and emit coherent radiation via inter- and intra-band electronic transitions in the solid.¹⁻⁴ This coherent emission occurs as bursts of attosecond pulses that have been observed as a harmonic comb in the frequency domain. Since its first experimental observation,⁵ considerable efforts were devoted to the

understanding of the main mechanisms behind high-order harmonic generation in solids (HHG). This new source of extreme ultraviolet (XUV) radiation^{6,7} displays a high degree of coherence,⁸ for instance, suitable for lensless diffractive imaging.⁹ It recently provided beams carrying orbital angular momentum with a selective topological charge.¹⁰ Recent studies also reveal that the HHG spatiotemporal properties are intricate due to the complex light-driven electronic

dynamics inside the solid. Hence, as a basic application, HHG can reveal information about the crystal's electronic band structure and intrinsic crystal properties.^{4,11} Future applications will exploit the ability to manipulate the light-driven electron motion during the crystal HHG process to create optoelectronic devices operating at petahertz frequencies^{12–14} or to extract topological information.¹⁵ However, increasing the yield is a prerequisite for the development of a solid-state HHG source and its applications. Various experimental techniques, such as plasmon-,^{16,17} waveguide-,^{9,18,19} and antenna-enhanced HHG,²⁰ were already implemented to achieve this goal. Here, we propose an alternative way of boosting the HHG yield from solids based on defects. This approach exploits the modification and control of the active medium's electronic structure to tailor the high-order harmonic output signal. Since defects are a cornerstone of most modern electronic devices, it appears promising to investigate their influence on the HHG yield. The addition of dopants creates electronic states in the bandgap, leading to modifications of the electronic band structure^{21,22} and bandgaps,^{23–26} allowing additional optical transitions.²⁷ Another significant effect of doping is the appearance of point defects such as vacancies and interstitial sites.^{28,29} According to recent theoretical investigations, dopant-induced bandgap changes can substantially influence the HHG process.^{29–33} In particular, donor-doped materials were theoretically predicted to enhance the HHG yield due to electronic excitation from impurity states.^{31,33}

We here investigate the influence of dopant-induced vacancies on the HHG yield in chromium-doped magnesium oxide (MgO:Cr), which was extensively studied previously using experimental^{34–37} and numerical^{38–40} methods. The Cr donor-dopants were found not only to substitute atoms with Cr³⁺ ions in the MgO lattice providing additional electrons but also to cause the formation of vacancies^{34–37} in order to maintain charge neutrality.³⁷

The HHG process in gases is well explained by the semi-classical “three-step model.”^{41–43} A similar approach has been proposed in crystals, where a strong laser electric field generates electron-hole pairs, which are subsequently accelerated by this field and emit radiation via inter- and intra-band opto-electronic transitions in the solid.^{1–4} The competition between those two mechanisms depends on the material. As a general feature, the driving laser parameters and, as a general feature, intra-band emission dominate at lower and inter-band emission at higher HHG photon energies, the latter including the plateau and cutoff domain of the HHG spectrum.

Figure 1 presents a scheme of the basic mechanisms involved in the HHG process in pristine and doped MgO. Here, the Cr donor-dopants not only substitute Mg atoms with Cr³⁺ ions in the MgO lattice, providing additional electrons [see Figs. 1(a) and 1(b)] but also cause the formation of vacancies^{34–37} to maintain charge neutrality.³⁷ The underlying electronic excitations in pristine and Cr-doped MgO are sketched in Figs. 1(c) and 1(d), respectively. An electron wave packet is (1) excited from the valence band (VB) to the first conduction band (CB1) with an initial field-dressed crystal momentum at the minimum bandgap (referred to as the Γ -point), where it (2) experiences intra-band acceleration. In case the laser electric field is strong enough, an electron wave packet is excited to a higher conduction band (CB2), where intra-band acceleration occurs, before (3) de-exciting to the VB upon recombination with its residual hole, emitting harmonics with photon energies equal to the instantaneous gap in the first BZ.

Within the Keldysh model for strong-field ionization⁴⁴ and a saddle-point analysis,^{45,46} a closed-form semi-quantitative approximation for the above bandgap (inter-band transition) yield is given by^{47,48}

$$Y_{\text{MgO}}(E) \propto \exp \left[-\frac{\sqrt{8 m_{vb-cb1}^*} \varepsilon_g^{3/2}}{e \hbar E} \right], \quad (1)$$

where $m_{vb-cb1}^* = (|\frac{1}{m_{vb}^*}| + |\frac{1}{m_{cb1}^*}|)^{-1}$ is the reduced effective mass of the VB and CB1, given in terms of their respective effective masses, m_{vb}^* and m_{cb1}^* , ε_g is the minimum bandgap energy between VB and CB1, and E is the peak field strength of the driving laser pulse. Similarly, we can account for excitations to higher conduction bands, e.g., to CB2 in our calculations, as sketched in Figs. 1(c) and 1(d), leading to the emission of harmonics at higher frequencies upon recombination to the VB. For a fixed driving electric-field amplitude, Eq. (1) predicts that a decrease in the minimum bandgap or reduced effective mass increases the HHG spectral yield above the minimum bandgap. Note that the effective electron mass is a crucial parameter, responsible for the electron mobility in solids. Its energy-dependent behavior was recently investigated.^{49,50} Since the Cr impurities with associated vacancies break the transitional symmetry of the MgO crystal (in the BZ of the pristine crystal), impurity levels couple with states of the valence and conduction bands along the entire BZ. Together with the dispersion-free-electron nature of MgO impurity levels,^{29,51,52} which implies a very large effective mass, the loss of symmetry allows us to represent impurity levels as flatbands in the BZ of the pristine sample [shown as extended horizontal lines in Figs. 1(c) and 1(d)]. The impurity-defect band (IDB) appears close to the CB1, and the vacancy defect band (VDB) emerges close to the VB. Adapting Eq. (1) to transitions from the VDB in MgO:Cr, we obtain the estimate for VDB contributions to the HHG yield

$$Y_{\text{MgO:Cr}}(E) \propto \exp \left[-\frac{\sqrt{8 m_{vdb-cb1}^*} (\varepsilon_{cb1} - \varepsilon_{vdb})^{3/2}}{e \hbar E} \right], \quad (2)$$

where $m_{vdb-cb1}^*$ is the reduced effective mass between CB1 and VDB. Because of the large VDB effective mass, we can approximate $m_{vdb-cb1}^* \approx m_{cb1}^* > m_{vb-cb1}^*$. Thus, the reduced effective mass is greater than that for the pristine sample. Nevertheless, because of the reduction of the bandgap induced by the vacancy, the numerator of the exponential in Eq. (2) is smaller than in Eq. (1), suggesting an enhancement of the HHG yield due to symmetry-allowed VDB–CB1 optical transitions.

For a fully quantitative description of HHG from pristine and doped MgO, we numerically solve the semiconductor Bloch equations (SBEs), including the VB, IDB, CB1, and CB2 (for details, see supplementary material SI.3). Disregarding temperature effects, the Fermi energy of MgO:Cr lies approximately between VDB and CB1,⁵³ so that the VB and VDB are initially occupied.

Figures 2(a) and 2(b) show the calculated HHG spectra from MgO and MgO:Cr, respectively. Both spectra are composed of odd harmonics (except for a dim even harmonic for the calculated spectra from MgO:Cr) and exhibit almost the same field-strength dependence of the cutoff. The main difference between them is the increased inter-band harmonic spectral yield at above-bandgap photon energies for the material with vacancy defects. We analyze the HHG-yield

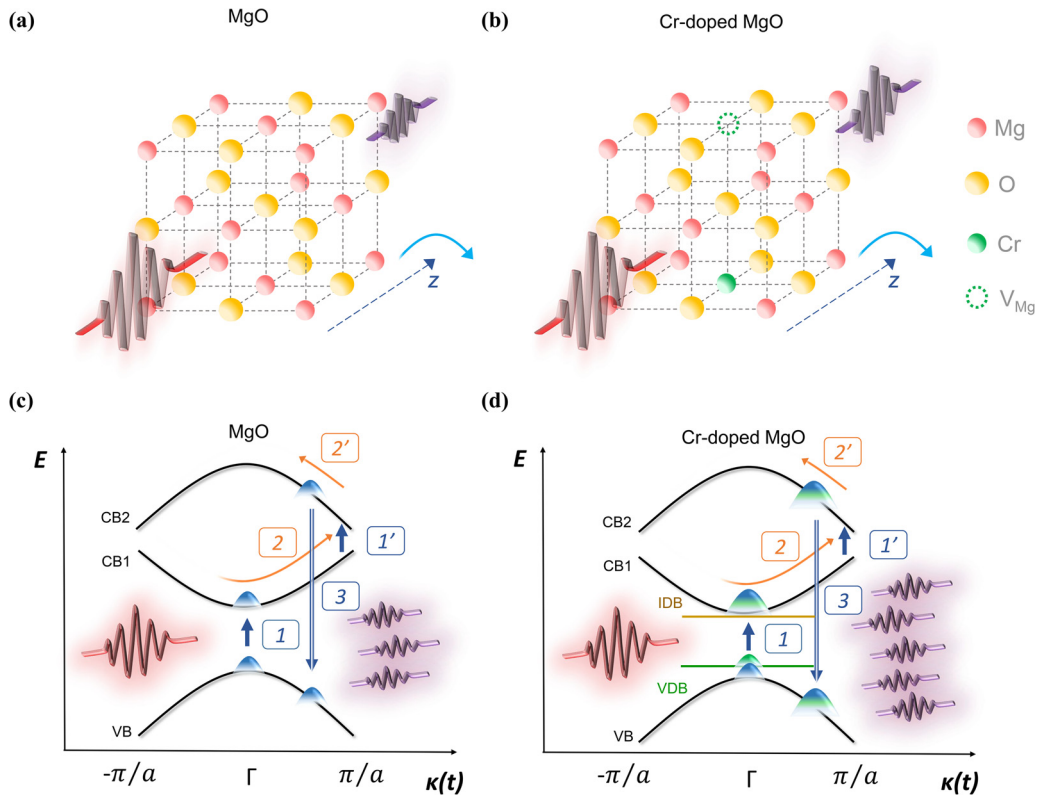


FIG. 1. Schematic of HHG in (a) and (c) MgO and (b) and (d) MgO:Cr in (a) and (b) coordinate and (c) and (d) momentum space. In (a) and (b), the laser propagation axis is indicated as z, around which crystals are rotated (light blue arrow) during anisotropy measurements [cf. Figs. 4(a) and 4(b)]. (b) A Mg vacancy replaces the closest Mg^{2+} ion along the [100] (C_{4v} symmetry) or [110] direction (C_{2v} symmetry). Both C_{4v} and C_{2v} centers are observed experimentally.^{27,34} (c) and (d) The laser electric field excites an electron wave packet from the valence band (VB) to the first conduction band (CB1) (1, blue arrow), where it experiences intra-band acceleration (2, orange arrow). At higher driver intensities, excitation to (1', blue arrow) and acceleration in (2', orange arrow) higher conduction bands (here CB2) can occur. The excited electron wave packet de-excites to the VB upon recombination with its residual hole (3, blue arrow), emitting harmonics of energy equal to the instantaneous energy in the first BZ. (d) In MgO:Cr, the occupied impurity defect band (IDB) and vacancy defect band (VDB) account for additional electronic transitions that enhance the net high-harmonic yield relative to MgO.

enhancement by comparing the spectra in Figs. 2(a) and 2(b) with our experimental data, estimating the intensity of the driving electric field inside the solids as detailed in the supplementary material SI.7. Our laser field is sufficiently strong to excite electrons to the CB2, leading

to the emission of harmonics in the XUV spectral range. Note that the consistent modeling of macroscopic optical effects, and the driving-laser field strength in matter, would require merging our theoretical model with Maxwell's equations, which is beyond the scope of the

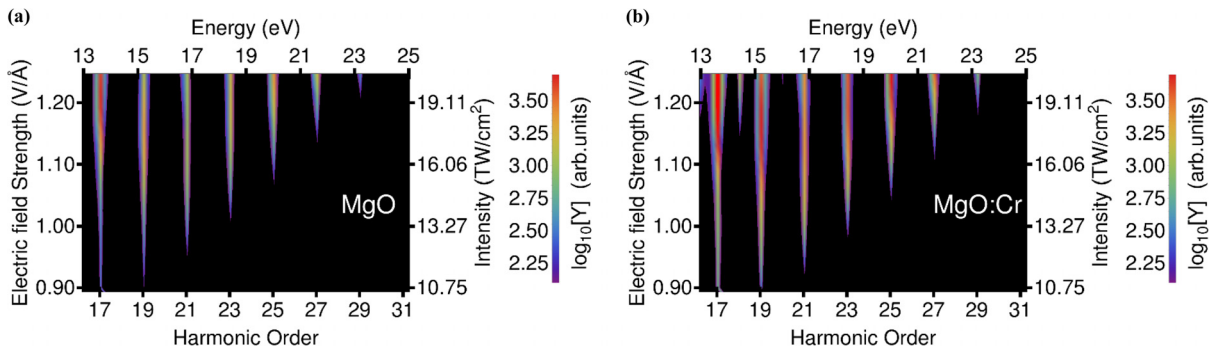


FIG. 2. Calculated HHG spectra from (a) MgO and (b) MgO:Cr crystals for driving laser-pulse incidence and HHG emission in $\Gamma - X$ direction as a function of the driver peak field strength. The laser central wavelength is $1.55 \mu\text{m}$ (corresponding to a photon energy of 0.80 eV, for details on the experimental parameters, see the supplementary material SI.5). Although the HHG yield from MgO:Cr is larger, we do not find evidence for a HHG cutoff extension for the doped sample.

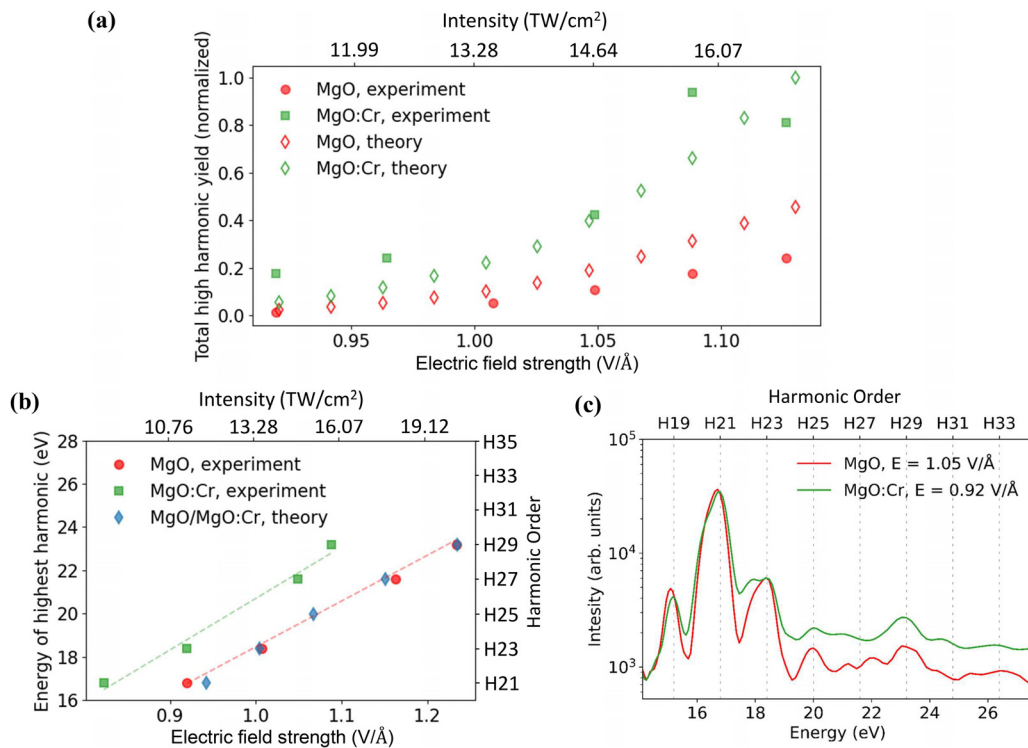


FIG. 3. Comparison of HHG signals from MgO and MgO:Cr crystals for a driving laser central wavelength of $1.55 \mu\text{m}$ (corresponding to a photon energy of 0.80 eV), (a) measured and calculated total harmonic yields in the $\Gamma - X$ direction, integrated over photon energies between 14.4 and 25.6 eV , as a function of the peak driving laser-electric-field strength. The integrated HHG yield from MgO:Cr crystal is larger. (b) Highest observable harmonic energy vs the driving field strength in the $\Gamma - X$ direction. The offset of the observed highest harmonic in both spectra is about 2 eV over a broad range of laser-electric-field strengths. It approximately matches the bandgap-energy difference between doped and undoped crystals. Dashed and solid lines are linear interpolations added to guide the eye. (c) Experimental HHG spectra obtained from MgO at a vacuum laser field strength of 1.05 V/\AA (14.6 TW/cm^2) and from MgO:Cr at a vacuum laser field strength of 0.92 V/\AA (11.2 TW/cm^2). In MgO:Cr, a weaker laser electric field results in a comparable integrated HHG yield.

current manuscript. Spectral transmission aspects are addressed in [supplementary material SI.2](#). The setup, intensity estimation, and the detailed description of the samples are given as [supplementary material](#). Both crystals, MgO and MgO:Cr, are $200\text{-}\mu\text{m}$ -thick with (001) oriented surfaces. We confirm the presence of Cr^{3+} ions in the MgO:Cr sample by photoluminescence measurements ([supplementary material SI.1](#)). In addition, the calculated densities of states (DOS) for MgO and MgO:Cr reveal defect states above the topmost valence band in MgO:Cr ([supplementary material SI.4](#)). Our transmission measurements show a bandgap-energy reduction of 1.8 eV in MgO:Cr, compared to the pure MgO bandgap energy of 7.16 eV ([supplementary material SI.2](#)).

Figure 3(a) shows the dependence of the experimental harmonic yield, integrated between 14.4 and 25.6 eV , on the driving laser electric-field strength. The total HHG yield from MgO:Cr is found to be larger than the one of pure MgO, up to a laser-field strength of about 1.15 V/\AA (corresponding to an intensity of 18 TW/cm^2). Operating at a repetition rate of 125 kHz , the damage threshold is reached at a laser electric-field strength of 1.23 V/\AA (20 TW/cm^2) and 1.09 V/\AA (15.7 TW/cm^2) for pure MgO and MgO:Cr, respectively. The lower damage threshold of MgO:Cr is probably associated with the increased electron density. In comparison, Fig. 3(a) presents the

numerically calculated intensities of odd harmonics for MgO and MgO:Cr, integrated over the same energy range. Our simulation results show good agreement with the experiment for pristine MgO and two discrepancies for doped MgO: (i) the experimental data show high harmonic emission starting at much lower laser-field strength, 0.71 V/\AA (6.74 TW/cm^2), with a smaller slope than that obtained from the simulations based on the solution of SBEs for doped MgO, (ii) the saturation of the HHG emission from MgO:Cr observed in the experiment is not reproduced by theory, since it involves mechanisms, such as radiation damage, which are not taken into account in the simulation. In spite of this, both measured and calculated results exhibit a pronounced increase in the HHG spectral intensity from the MgO:Cr crystal, as the result of added transitions from the VDB.

Figure 3(b) shows the highest harmonic order we are able to detect for driving-laser-field strengths (in vacuum) between 0.82 V/\AA (9 TW/cm^2) and 1.23 V/\AA (20 TW/cm^2) for both samples. It also shows HHG cutoffs retrieved from our calculated spectra in Figs. 2(a) and 2(b). Figure 3(b) shows a linear scaling of the highest experimentally detected harmonic as a function of the peak-electric-field strength in both MgO and MgO:Cr, with almost the same slope but an energy offset of approximately 2 eV . This energy offset is close to the bandgap-energy difference between MgO and MgO:Cr of $\approx 1.8 \text{ eV}$

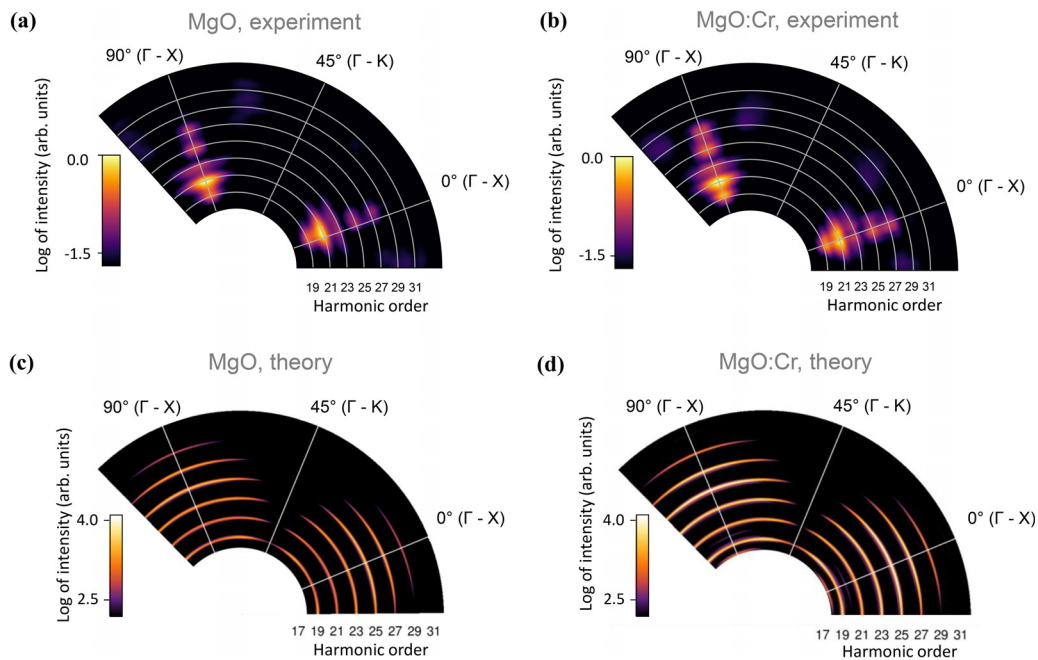


FIG. 4. Crystal-orientation dependence of HHG in (a) and (c) MgO and (b) and (d) MgO:Cr crystals. The crystals are rotated about the laser propagation axis [z axes in Figs. 1(a) and 1(b)] in 3° steps, whereas the linear laser polarization is kept fixed. Measured HHG spectra for (a) MgO at a peak laser-field strength (vacuum value) of 1.23 V/\AA (20 TW/cm^2) and (b) MgO:Cr at 1.09 V/\AA (15.7 TW/cm^2). Due to the low doping concentration (0.5%), the fourfold symmetry of the MgO cubic crystal structure is unaltered in MgO:Cr. Calculated spectra at 1.23 V/\AA for (c) MgO and (d) MgO:Cr.

that we experimentally determined independently using optical transmission measurements (supplementary material SI.2). The highest harmonic order obtained from the simulations in Figs. 2(a) and 2(b) is identical for MgO and MgO:Cr crystals. The extension of the highest experimentally observable harmonic from MgO:Cr is not obvious. Indeed, since for the same electric-field strength the electron wave packet explores the same region of the first BZ of the MgO and MgO:Cr crystals, one might expect identical HHG cutoffs. We attribute the measured apparent extension of the HHG spectra from MgO:Cr to a higher yield in the plateau region. To further illustrate the HHG behavior, Fig. 3(c) displays HHG spectra measured at a driving-laser peak field strength of 0.92 V/\AA (11.2 TW/cm^2) for MgO:Cr and of 1.05 V/\AA (14.6 TW/cm^2) for MgO. The two spectra have comparable yields even though the HHG spectrum from MgO:Cr was obtained at a lower laser field strength. This is in qualitative agreement with the simulated spectra displayed in Fig. 2. In addition, we notice in the experimental spectra that harmonics above 19 eV are less intense than those below this energy. This sharp transition between these two plateaus has been reported as a contribution from higher conduction bands associated with low population transfer.^{54,55}

Moreover, we consider the contribution of macroscopic effects. The driving laser propagation inside the crystal can play a significant role on its initial spatial or spectral properties and the emitted harmonic radiation.⁵⁶ Although the optical propagation effects related to the change of linear and nonlinear refractive indices due to doping are unlikely to play a significant role on the driving laser properties in our experiment, given the low dopant concentration of 0.5%,^{57–60} we

observe the difference of spatial and spectral properties of the harmonic beam from MgO and MgO:Cr. We detect a blueshift of the HHG spectra in MgO:Cr compared to HHG spectra from MgO at a fixed laser intensity (supplementary material SI.5). We associate this wavelength shift to the increased electron density participating in HHG from MgO:Cr. Since the plasma refractive index variation acts as a diverging lens in the spatial domain, we attribute the observed blueshift to plasma-induced defocusing of the fundamental beam (Refs. 61–63 and references therein). Further investigations in a loose geometry configuration or in reflection geometry would limit possible contributions of macroscopic effects.⁵⁶ In a more general context, other crystals and/or higher doping rates may induce larger macroscopic aspects, which may play a significant role in enhancement or in spectral or spatial modifications of the HHG properties.¹⁹

Next, we study the crystal-orientation-dependent HHG response of both crystals. To investigate the HHG anisotropy, we measure the HHG signal as a function of the crystal orientation with respect to the laser polarization, as sketched in Figs. 1(a) and 1(b) and described in supplementary material SI.5. Figures 4(a) and 4(b) present angle-dependent-measured HHG spectra from MgO and MgO:Cr, recorded at their respective optimal conditions for the highest HHG yields, i.e., just below the damage threshold at peak electric-field strengths of 1.23 V/\AA (20 TW/cm^2) for MgO and 1.09 V/\AA (15.7 TW/cm^2) for MgO:Cr. The fourfold symmetry reflects the face-centered cubic crystal structure of MgO.⁶⁴ The HHG yield is largest along the $\Gamma - X$ direction, while no signal is observed along the $\Gamma - K$ direction. Overall, the two anisotropy dependences are comparable, which is consistent with the fact that the crystal symmetry is preserved for our

low dopant concentrations. We observe that, similar to Fig. 3(a), the harmonics emitted from MgO:Cr have a comparable yield at lower driving-field intensities than harmonics from pure MgO. To analyze this behavior, we have calculated the angle-dependent HHG yield for MgO and MgO:Cr at the same peak vacuum electric-field strength of 1.23 V/\AA (20 TW/cm^2), as shown in Figs. 4(c) and 4(d). These calculations are performed in reduced dimensionality, representing the crystal as a 2D square lattice using the same model electronic potential as in recent works,^{2,65,66} $V(x, y) = V_0 \cos(ax) + V_0 \cos(ay)$, but allowing for a modified oscillation amplitude V_0 at the defect sites in MgO:Cr^{30,31,33,67,68} (supplementary material SI.3). Even though the angular spread of the harmonics differs between theory and experiment, we reproduce the maximal yields measured along the $\Gamma - X$ and the minimal yields along the $\Gamma - K$ direction. For all crystal orientations, our numerical simulation predicts a larger HHG yield for MgO:Cr. These two last characteristics are in good qualitative agreement with the present experimental findings.

In conclusion, we present the HHG yield enhancement from MgO doped with chromium atoms compared to a pure MgO crystal. We associate the extension of the highest observable harmonic in MgO:Cr to an increase in the HHG plateau intensity. The HHG-yield increase from the doped crystal is interpreted as optical excitations introduced by occupied defect states in MgO:Cr that arise from Cr^{3+} dopant ions and Mg-vacancy formation in the MgO lattice. This finding is in agreement with our numerical simulations and previous theoretical predictions of enhanced HHG in doped samples.^{30,31,33,67} The HHG anisotropy shows that the pristine MgO crystal symmetry is preserved upon doping. Our numerical results do not reproduce the experimentally observed HHG spectral blue shift and saturation, both caused by additional free electrons in the doped MgO, which we attribute to our incomplete description of the driving laser pulse in the solid. Other crystals involved in the HHG or other dopant concentrations may enhance macroscopic effects that could be exploited to boost the HHG yield in specific spectral ranges. As a perspective, our study promotes the development of efficient compact XUV light sources based on doping. Moreover, it has been suggested that HHG from crystals with defects can provide a way to study dipole moments and wave functions of impurity arrangements⁶⁸ and, thus, potentially serve as a tomographic measurement of impurity orbitals. Other future studies will concentrate on HHG spectroscopy to extract information on the intrinsic properties of light-driven attosecond electron transport.⁶⁹ This would create attractive perspectives toward the development of all-solid-state attosecond sources and petahertz electronics.^{12-14,29-33,55}

See the supplementary material for the details on the photoluminescence measurements and optical characterization and properties of pristine and chromium-doped MgO; on the detailed description of the theoretical model for HHG in solids with vacancy defects as well as the appearance of vacancy-induced defect states in MgO:Cr from density functional theory; on the description of experimental setup and comparison of the obtained HHG spectra; and on OPCA laser system as well as on laser intensity estimation and notation.

The authors thank M. Billon for technical support. We acknowledge support from the PETACOM (Petahertz Optoelectronics Communication) FET Open H2020 Grant No. 829153, OPTOLogic

(Optical Topologic Logic) FET Open H2020 Grant No. 899794, support from the French ANR through the grant PACHA (No. ANR-17-CE30-0008-01) and the labex PALM (No. ANR-10-LABX-0039-PALM), support the DGA RAPID grant "SWIM." We acknowledge the financial support from the French ASTRE program through the "NanoLight" grant, the Spanish Ministry MINECO (National Plan 15 grant: FISICATEAMO No. FIS2016-79508-P, SEVERO OCHOA No. SEV-2015-0522, FPI), European Social Fund, Fundació Cellex, Fundació Mir-Puig, Generalitat de Catalunya (AGAUR Grant No. 2017 SGR 1341, CERCA/Program), ERC AdG NOQIA, EU FEDER, European Union Regional Development Fund-ERDF Operational Program of Catalonia 2014–2020 (Operation Code: IU16-011424), MINECO-EU QUANTERA MAQS [funded by The State Research Agency (AEI) No. PCI2019-111828-2/10.13039/501100011033], and the National Science Centre, Poland-Symfonia Grant No. 2016/20/W/ST4/00314. F.N. and U.T. acknowledge support from Air Force Office of Scientific Research under Award No. FA9550-17-1-0369 and NSF Grant No. 1802085 (theory for photoemission from surfaces). Any opinions, findings, and conclusions or recommendations expressed in this material are those of the authors and do not necessarily reflect the views of the United States Air Force. U.T. acknowledges partial support from the Chemical Sciences, Geosciences, and Biosciences Division, Office of Basic Energy Sciences, Office of Science, US Department of Energy under Award No. DEFG02-86ER13491. N.T.-D. thanks A. Rubio.

DATA AVAILABILITY

The data that support the findings of this study are available within the article and its supplementary material.

REFERENCES

- ¹S. Ghimire, A. D. DiChiara, E. Sistrunk, G. Ndashimiye, U. B. Szafruga, A. Mohammad, P. Agostini, L. F. DiMauro, and D. A. Reis, "Generation and propagation of high-order harmonics in crystals," *Phys. Rev. A* **85**, 043836 (2012).
- ²G. Vampa, C. R. McDonald, G. Orlando, D. D. Klug, P. B. Corkum, and T. Brabec, "Theoretical analysis of high-harmonic generation in solids," *Phys. Rev. Lett.* **113**, 073901 (2014).
- ³T. T. Luu and H. J. Wörner, "High-order harmonic generation in solids: A unifying approach," *Phys. Rev. B* **94**, 115164 (2016).
- ⁴N. Tancogne-Dejean, O. D. Mücke, F. X. Kärtner, and A. Rubio, "Impact of the electronic band structure in high-harmonic generation spectra of solids," *Phys. Rev. Lett.* **118**, 087403 (2017).
- ⁵S. Ghimire, A. D. DiChiara, E. Sistrunk, P. Agostini, L. F. DiMauro, and D. A. Reis, "Observation of high-order harmonic generation in a bulk crystal," *Nat. Phys.* **7**, 138 (2011).
- ⁶G. Vampa, C. McDonald, A. Fraser, and T. Brabec, "High-harmonic generation in solids: Bridging the gap between attosecond science and condensed matter physics," *IEEE J. Sel. Top. Quantum Electron.* **21**, 8700110 (2015).
- ⁷M. Garg, M. Zhan, T. T. Luu, H. Lakhota, T. Klostermann, A. Guggenmos, and E. Goulielmakis, "Multi-petahertz electronic metrology," *Nature* **538**, 359 (2016).
- ⁸H. Kim, S. Han, Y. W. Kim, S. Kim, and S.-W. Kim, "Generation of coherent extreme-ultraviolet radiation from bulk sapphire crystal," *ACS Photonics* **4**, 1627 (2017).
- ⁹D. Franz, S. Kaassamani, D. Gauthier, R. Nicolas, M. Kholodtsova, L. Douillard, J.-T. Gomes, L. Lavoute, D. Gaponov, N. Ducros, S. Février, J. Biegert, L. Shi, M. Kovačev, W. Boutou, and H. Merdji, "All semiconductor enhanced high-harmonic generation from a single nanostructured cone," *Sci. Rep.* **9**, 5663 (2019).

- ¹⁰D. Gauthier, S. Kaassamani, D. Franz, R. Nicolas, J.-T. Gomes, L. Lavoute, D. Gaponov, S. Février, G. Jargot, M. Hanna, W. Boutu, and H. Merdji, "Orbital angular momentum from semiconductor high-order harmonics," *Opt. Lett.* **44**, 546 (2019).
- ¹¹A. A. Lanin, E. A. Stepanov, A. B. Fedotov, and A. M. Zheltikov, "Mapping the electron band structure by intraband high-harmonic generation in solids," *Optica* **4**, 516 (2017).
- ¹²F. Krausz and M. I. Stockman, "Attosecond metrology: From electron capture to future signal processing," *Nat. Photonics* **8**, 205 (2014).
- ¹³J. Schoetz, Z. Wang, E. Pisanty, M. Lewenstein, M. F. Kling, and M. F. Ciappina, "Perspective on petahertz electronics and attosecond nanoscopy," *ACS Photonics* **6**, 3057 (2019).
- ¹⁴S. Sederberg, D. Zimin, S. Keiber, F. Siegrist, M. S. Wismer, V. S. Yakovlev, I. Floss, C. Lemell, J. Burgdörfer, M. Schultze, F. Krausz, and N. Karpowicz, "Attosecond optoelectronic field measurement in solids," *Nat. Commun.* **11**, 430 (2020).
- ¹⁵R. E. F. Silva, A. Jiménez-Galán, B. Amorim, O. Smirnova, and M. Ivanov, "Topological strong-field physics on sub-laser-cycle timescale," *Nat. Photonics* **13**, 849 (2019).
- ¹⁶S. Han, H. Kim, Y.-W. Kim, Y.-J. Kim, S. Kim, I.-Y. Park, and S.-W. Kim, "High-harmonic generation by field enhanced femtosecond pulses in metal-sapphire nanostructure," *Nat. Commun.* **7**, 13105 (2016).
- ¹⁷G. Vampa, B. G. Ghamsari, S. Siadat Mousavi, T. J. Hammond, A. Olivieri, E. Lisicka-Skretek, A. Y. Naumov, D. M. Villeneuve, A. Staudte, P. Berini, and P. B. Corkum, "Plasmon-enhanced high-harmonic generation from silicon," *Nat. Phys.* **13**, 659 (2017).
- ¹⁸D. Franz, R. Nicolas, W. Boutu, L. Shi, Q. Ripault, M. Kholodtsova, B. Iwan, U. E. Etxano, M. Kovacev, J. Biegert, and H. Merdji, "Amplification of high harmonics in 3d semiconductor waveguides," [arXiv:09153v1](https://arxiv.org/abs/09153v1) (2017).
- ¹⁹M. Siviš, M. Taucer, G. Vampa, K. Johnston, A. Staudte, A. Naumov, D. Villeneuve, C. Ropers, and P. Corkum, "Tailored semiconductors for high-harmonic optoelectronics," *Science* **357**, 303 (2017).
- ²⁰K. Imasaka, T. Kaji, T. Shimura, and S. Ashihara, "Antenna-enhanced high harmonic generation in a wide-bandgap semiconductor ZnO," *Opt. Express* **26**, 21364 (2018).
- ²¹T. Umebayashi, T. Yamaki, H. Itoh, and K. Asai, "Band gap narrowing of titanium dioxide by sulfur doping," *Appl. Phys. Lett.* **81**, 454 (2002).
- ²²N. Kamarulzaman, M. F. Kasim, and N. F. Chayed, "Elucidation of the highest valence band and lowest conduction band shifts using XPS for ZnO and Zn_{0.99}Cu_{0.01}O band gap changes," *Results Phys.* **6**, 217 (2016).
- ²³D. Auvergne, J. Camassel, and H. Mathieu, "Band-gap shrinkage of semiconductors," *Phys. Rev. B* **11**, 2251 (1975).
- ²⁴H. J. Queisser and E. E. Haller, "Defects in semiconductors: Some fatal, some vital," *Science* **281**, 945 (1998).
- ²⁵F. Oba and Y. Kumagai, "Design and exploration of semiconductors from first principles: A review of recent advances," *Appl. Phys. Express* **11**, 060101 (2018).
- ²⁶C. Di Valentin and G. Pacchioni, "Spectroscopic properties of doped and defective semiconducting oxides from hybrid density functional calculations," *Acc. Chem. Res.* **47**, 3233 (2014).
- ²⁷B. Henderson and G. F. Imbusch, *Optical Spectroscopy of Inorganic Solids* (Oxford University Press, 1989), Vol. 23, p. 2824.
- ²⁸A. V. Chadwick and M. Terenzi, *Defects in Solids: Modern Techniques* (Springer Science & Business Media, 2013), Vol. 23, p. 2824.
- ²⁹M. S. Mrudul, N. Tancogne-Dejean, A. Rubio, and G. Dixit, "High-harmonic generation from spin-polarised defects in solids," *npj Comput. Mater.* **6**, 10 (2020).
- ³⁰T. Huang, X. Zhu, L. Li, X. Liu, P. Lan, and P. Lu, "High-order-harmonic generation of a doped semiconductor," *Phys. Rev. A* **96**, 043425 (2017).
- ³¹C. Yu, K. K. Hansen, and L. B. Madsen, "Enhanced high-order harmonic generation in donor-doped band-gap materials," *Phys. Rev. A* **99**, 013435 (2019).
- ³²X.-F. Pan, T. Han, C.-L. Xia, T.-T. Xu, J. Zhang, and X.-S. Liu, "Energy band splitting and high-order harmonic generation from a doped semiconductor," *Laser Phys. Lett.* **16**, 115301 (2019).
- ³³H. Irvani, K. K. Hansen, and L. B. Madsen, "Effects of vacancies on high-order harmonic generation in a linear chain with band gap," *Phys. Rev. Res.* **2**, 013204 (2020).
- ³⁴M. O. Henry, J. P. Larkin, and G. F. Imbusch, "Nature of the broadband luminescence center in MgO:Cr³⁺," *Phys. Rev. B* **13**, 1893 (1976).
- ³⁵J. B. Wachtman and A. D. E. Franklin, "Mass transport in oxides," in *Proceedings of a Symposium*, Gaithersburg, Maryland, October 22–25, 1967 (1968), Vol. 13, p. 12.
- ³⁶F. Stavale, N. Nilius, and H.-J. Freund, "Cathodoluminescence of near-surface centres in Cr-doped MgO(001) thin films probed by scanning tunnelling microscopy," *New J. Phys.* **14**, 033006 (2012).
- ³⁷E. Shablonin, A. I. Popov, A. Lushchik, A. Kotlov, and S. Dolgova, "Excitation of different chromium centres by synchrotron radiation in MgO:Cr single crystals," *Physica B* **477**, 133 (2015).
- ³⁸J. Aramburu, P. García-Fernández, M. Barriuso, and M. Moreno, "Transition metal complexes coupled to vacancies in oxides: Origin of different properties of Cr³⁺ in MgO bounded to a <100> or <110> Mg²⁺ vacancy," *J. Phys. Chem. A* **117**, 12642 (2013).
- ³⁹J. Aramburu, P. Garcia-Fernandez, J. Garcia-Lastra, M. Barriuso, and M. Moreno, "Colour due to Cr³⁺ ions in oxides: A study of the model system MgO:Cr³⁺," *J. Phys.* **25**, 175501 (2013).
- ⁴⁰M. Novita and K. Ogasawara, "Study on multiplet energies of V²⁺, Cr³⁺, and Mn⁴⁺ in MgO host crystal based on first-principles calculations with consideration of lattice relaxation," *J. Phys. Soc. Jpn.* **83**, 124707 (2014).
- ⁴¹J. L. Krause, K. J. Schafer, and K. C. Kulander, "High-order harmonic generation from atoms and ions in the high intensity regime," *Phys. Rev. Lett.* **68**, 3535 (1992).
- ⁴²P. B. Corkum, "Plasma perspective on strong field multiphoton ionization," *Phys. Rev. Lett.* **71**, 1994 (1993).
- ⁴³K. C. Kulander, K. J. Schafer, and J. L. Krause, "Dynamics of short-pulse excitation, ionization and harmonic conversion," in *Super-Intense Laser-Atom Physics*, NATO ASI Series (Series B: Physics), Vol. 316, edited by B. Piraux, A. L'Huillier, and K. Rzażewski (Springer, Boston, MA, 1993).
- ⁴⁴L. V. Keldysh, "Ionization in the field of a strong electromagnetic wave," *Sov. Phys. JETP* **20**, 1307 (1965).
- ⁴⁵M. Lewenstein, P. Balcou, M. Y. Ivanov, A. L'Huillier, and P. B. Corkum, "Theory of high-harmonic generation by low-frequency laser fields," *Phys. Rev. A* **49**, 2117 (1994).
- ⁴⁶R. Wong, *Asymptotic Approximations of Integrals*, Classics in Applied Mathematics Vol. 34 (Society of Industrial and Applied Mathematics, 2001).
- ⁴⁷F. Navarrete, M. F. Ciappina, and U. Thumm, "Crystal-momentum-resolved contributions to high-order harmonic generation in solids," *Phys. Rev. A* **100**, 033405 (2019).
- ⁴⁸F. Navarrete and U. Thumm, "Two-color-driven enhanced high-order harmonic generation in solids," *Phys. Rev. A* **102**, 063123 (2020).
- ⁴⁹L. Kasmí, M. Lucchini, L. Castiglioni, P. Kliuiev, J. Osterwalder, M. Hengsberger, L. Gallmann, P. Krüger, and U. Keller, "Effective mass effect in attosecond electron transport," *Optica* **4**, 1492 (2017).
- ⁵⁰M. J. Ambrosio and U. Thumm, "Spatiotemporal analysis of a final-state shape resonance in interferometric photoemission from Cu(111) surfaces," *Phys. Rev. A* **100**, 043412 (2019).
- ⁵¹P. V. C. Medeiros, S. Stafström, and J. Björk, "Effects of extrinsic and intrinsic perturbations on the electronic structure of graphene: Retaining an effective primitive cell band structure by band unfolding," *Phys. Rev. B* **89**, 041407 (2014).
- ⁵²M. Hjort and S. Stafström, "Modeling vacancies in graphite via the Hückel method," *Phys. Rev. B* **61**, 14089 (2000).
- ⁵³C. Kittel, *Quantum Theory of Solids* (Wiley, 1987).
- ⁵⁴A. J. Uzan, G. Orenstein, A. Jiménez-Galán, C. McDonald, R. E. F. Silva, B. D. Bruner, N. D. Klimkin, V. Blanchet, T. Arusi-Parpar, M. Krüger, A. N. Rubtsov, O. Smirnova, M. Ivanov, B. Yan, T. Brabec, and N. Dudovich, "Attosecond spectral singularities in solid-state high-harmonic generation," *Nat. Photonics* **14**, 183 (2020).
- ⁵⁵Y. S. You, M. Wu, Y. Yin, A. Chew, X. Ren, S. Gholam-Mirzaei, D. A. Browne, M. Chini, Z. Chang, K. J. Schafer, M. B. Gaarde, and S. Ghimire, "Laser waveform control of extreme ultraviolet high harmonics from solids," *Opt. Lett.* **42**, 1816 (2017).
- ⁵⁶G. Vampa, Y. S. You, H. Liu, S. Ghimire, and D. A. Reis, "Observation of backward high-harmonic emission from solids," *Opt. Express* **26**, 12210 (2018).
- ⁵⁷A. Miller and D. Finlayson, *Laser Sources and Applications* (CRC Press, 1997), p. 315.
- ⁵⁸M. Lai, J. Nicholson, and W. Rudolph, "Multiple pulse operation of a femtosecond Ti: sapphire laser," *Opt. Commun.* **142**, 45 (1997).

- ⁵⁹J. Philip, C. D'Amico, G. Cheriaux, A. Couairon, B. Prade, and A. Mysyrowicz, "Amplification of femtosecond laser filaments in Ti:sapphire," *Phys. Rev. Lett.* **95**, 163901 (2005).
- ⁶⁰Y. Guo, S. Lu, L. Su, C. Zhao, H. Zhang, and S. Wen, "Z-scan measurement of the nonlinear refractive index of Nd³⁺, Y³⁺-codoped CaF₂ and SrF₂ crystals," *Appl. Opt.* **54**, 953 (2015).
- ⁶¹S. C. Rae, "Spectral blueshifting and spatial defocusing of intense laser pulses in dense gases," *Opt. Commun.* **104**, 330 (1994).
- ⁶²A. Heins, S. C. Singh, and C. Guo, "Electron kinetic energy and plasma emission diagnosis from femtosecond laser produced air plasmas," *Phys. Plasmas* **24**, 072101 (2017).
- ⁶³V. E. Nefedova, M. F. Ciappina, O. Finke, M. Albrecht, J. Vábek, M. Kozlová, N. Suárez, E. Pisanty, M. Lewenstein, and J. Nejd, "Determination of the spectral variation origin in high-order harmonic generation in noble gases," *Phys. Rev. A* **98**, 033414 (2018).
- ⁶⁴Y. S. You, D. Reis, and S. Ghimire, "Anisotropic high-harmonic generation in bulk crystals," *Nat. Phys.* **13**, 345 (2017).
- ⁶⁵M. Wu, S. Ghimire, D. A. Reis, K. J. Schafer, and M. B. Gaarde, "High-harmonic generation from Bloch electrons in solids," *Phys. Rev. A* **91**, 043839 (2015).
- ⁶⁶X. Liu, X. Zhu, P. Lan, X. Zhang, D. Wang, Q. Zhang, and P. Lu, "Time-dependent population imaging for high-order-harmonic generation in solids," *Phys. Rev. A* **95**, 063419 (2017).
- ⁶⁷A. Pattanayak, M. M. S , and G. Dixit, "Influence of vacancy defects in solid high-order harmonic generation," *Phys. Rev. A* **101**, 013404 (2020).
- ⁶⁸S. Almalki, A. M. Parks, G. Bart, P. B. Corkum, T. Brabec, and C. R. McDonald, "High harmonic generation tomography of impurities in solids: Conceptual analysis," *Phys. Rev. B* **98**, 144307 (2018).
- ⁶⁹Q. Liao, W. Cao, Q. Zhang, K. Liu, F. Wang, P. Lu, and U. Thumm, "Distinction of electron dispersion in time-resolved photoemission spectroscopy," *Phys. Rev. Lett.* **125**, 043201 (2020).

Enhanced extreme ultraviolet high-harmonic generation from chromium-doped magnesium oxide

V. E. Nefedova,¹ S. Fröhlich,¹ F. Navarrete,^{2,3} N. Tancogne-Dejean,⁴ D. Franz,¹ A. Hamdou,¹ S. Kaassamani,¹ D. Gauthier,¹ R. Nicolas,^{1,5} G. Jargot,^{6,7} M. Hanna,⁶ P. Georges,⁶ M. F. Ciappina,^{8,9,10} U. Thumm,^{2, a)} W. Boutu,¹ and H. Merdji^{1, b)}

¹⁾Ultrafast Nanophotonics group, LIDYL, CEA-CNRS-Université Paris-Saclay 91191, Gif-sur-Yvette, France

²⁾Department of Physics, Kansas State University, Manhattan, KS 66506, USA

³⁾Institute of Physics, University of Rostock, 18051 Rostock, Germany

⁴⁾Max Planck Institute for the Structure and Dynamics of Matter and Center for Free-Electron Laser Science, Luruper Chaussee 149, 22761 Hamburg, Germany

⁵⁾Department of Natural Sciences, Lebanese American University, 1102 Beirut, Lebanon

⁶⁾Université Paris-Saclay, Institut d'Optique Graduate School, CNRS, Laboratoire Charles Fabry, 91127, Palaiseau, France

⁷⁾Fastlite, 06600 Antibes, Sophia Antipolis, France

⁸⁾ICFO-Institut de Ciències Fotoniques, The Barcelona Institute of Science and Technology, Avenue Carl Friedrich Gauss 3, 08860 Castelldefels (Barcelona), Spain

⁹⁾Physics Program, Guangdong Technion – Israel Institute of Technology, Shantou, Guangdong 515063, China

¹⁰⁾Technion – Israel Institute of Technology, Haifa, 32000, Israel

(Dated: 12 April 2021)

SI.1. PHOTOLUMINESCENCE MEASUREMENTS ON MgO AND MgO:Cr

In order to confirm the presence of Cr^{3+} ions in the MgO:Cr crystal, we perform photoluminescence (PL) measurements on both, MgO and MgO:Cr samples, and compare the obtained signals. The PL measurements are done at room temperature with an excitation wavelength of 365 nm. The source signal is filtered out before the detection, using a long-pass filter with a cutoff wavelength of 514 nm. The PL signal is detected by a spectrometer (Ocean Optics QE Pro Spectrometer).

Figure S1 shows the PL signals from both samples. There is a strong PL signal from MgO:Cr, which consists of multiple peaks with a broad feature around 700 - 800 nm. Such a behavior of the PL signal is typically attributed to ${}^4T_2 \rightarrow {}^4A_2$ transitions from Cr^{3+} ions in orthorhombic sites in MgO^{1-3} . Therefore, our PL measurements experimentally confirm the presence of Cr^{3+} ions in the MgO:Cr sample, which lead to the formation of Mg vacancies. Photoluminescence measurements in MgO reveal peaks near 720 nm as well as around 850-950 nm. We attribute these features to impurities in the undoped MgO sample, the signal around 720 nm being probably associated with Cr impurities, while multiple lines around 850-950 nm may be due to $Mg(OH)_2$ contamination. A similar PL behavior from MgO undoped samples was reported in previous works⁴⁻⁸.

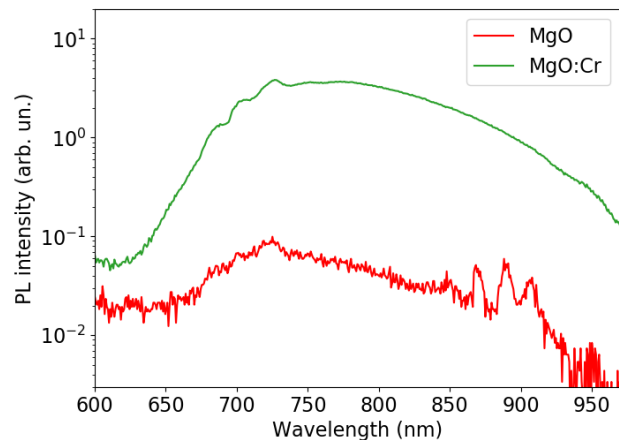


FIG. S1: Measured photoluminescence signal from the MgO and MgO:Cr samples excited at a wavelength of 365 nm at room temperature. Both curves are on the same scale.

SI.2. OPTICAL CHARACTERIZATION AND PROPERTIES OF PRISTINE AND CHROMIUM-DOPED MgO

In order to obtain information about the band-gap energies of our MgO and MgO:Cr samples with 5000 ppm chromium concentration (corresponding to $\sim 0.5\%$ defect concentration), we measure the transmission of white light through the samples. We apply the Tauc method of optical absorption-edge determination⁹. This method is used to determine the optical band gap in semiconductors. The obtained Tauc plots are shown in Fig. S2. The linear region of the curve has to

^{a)}Corresponding author, email address: thumm@phys.ksu.edu

^{b)}Corresponding author, email address: hamed.merdji@cea.fr

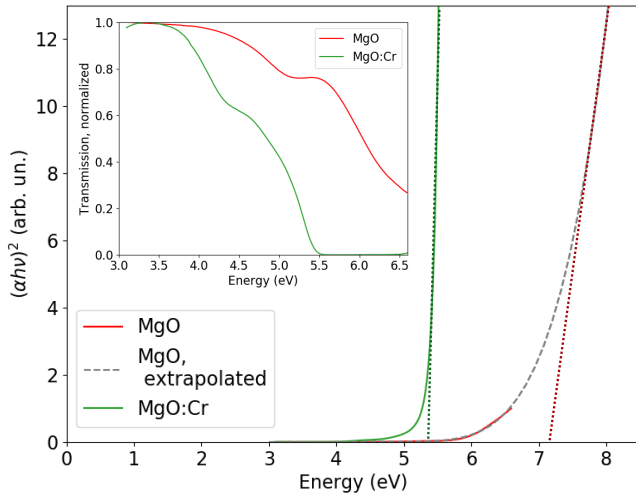


FIG. S2: Tauc plots (and transmission curves as an insert) of the MgO and MgO:Cr samples, where $h\nu$ is the photon energy and α the absorption coefficient (calculated from the measured transmission data).

be extrapolated for the determination of the band-gap energy. We infer from the data a band-gap energy for MgO:Cr of about 5.36 eV. The energy range of the detector is limited to a maximum photon energy of 6.52 eV. For energies above 6.52 eV, we use a fifth-order polynomial extrapolation in the Tauc plot. The linear region in the extrapolated Tauc plot for MgO provides a band-gap energy of 7.16 eV. The band-gap-energy difference between the doped and undoped crystals is around 1.8 eV. We note that the commonly used value for the band-gap energy of the pristine MgO is 7.8 eV¹⁰. The observed modification of the band structure, with the consequent band-gap narrowing in MgO:Cr compared to MgO, results from vacancies imposed by added Cr^{3+} ions in MgO that preserve charge neutrality^{11,12}.

In alkali halides, the exciton transitions near the cation vacancy are known to be responsible for the band-gap change^{13,14}. The possible presence of vacancy-induced exciton is difficult to determine precisely from our transmission data. The observed band-gap narrowing could be a combined effect of both: the presence of in-gap states and a vacancy-induced exciton. From the one hand, our DFT calculations provided in SI.4 confirm the effect of the bandgap reduction due to defect states in the bandgap. From another hand, the importance of the binding energy of the exciton for our samples is not yet determined. The possible role of excitonic effects on the band-gap modification of our samples is a subject for future investigations.

The optical properties of MgO crystal are given in Table S1 for the driving laser wavelength $\lambda = 1550$ nm as well as for two high harmonic orders in the HHG plateau spectral region, harmonic order 21 ($\lambda = 73.81$ nm; $E = 16.79$ eV) and 23 ($\lambda = 67.39$ nm; $E = 18.39$ eV). The complex refractive index n^* is given by $n^* = n_r + in_i$. The attenuation length (defined as the distance over which the intensity of the radiation drops to $1/e$ compared to the initial value) is given by¹⁵

	IR laser	HH ₂₁	HH ₂₃
λ (nm)	1550	73.81	67.39
n^*	$1.71 + 1 \times 10^{-6}i$	$1.31 + 0.98i$	$0.89 + 0.99i$
l_{at} (nm)	123×10^6	6.00	5.42

TABLE S1: Complex refractive index n^* and attenuation length l_{at} for MgO for the driving laser and harmonic orders 21 and 23.

$l_{at} = \lambda / 4\pi n_i$. According to the calculated data provided in Table S1, the attenuation length for XUV high-order harmonics in the MgO crystal is only few nanometers. Therefore, the detected high-order-harmonic radiation is produced from a very narrow layer at the rear side of the crystal.

While the n_i values in the XUV region are well established^{16,17}, the data at 1550 nm vary from few times 10^{-6} to 2×10^{-8} with the quality of the crystals¹⁷ (and references therein). Taking the upper limit of n_i as 1×10^{-6} results in an attenuation length of $l_{at} = 12.3$ mm. According to the Beer-Lambert law, the transmission of light through our crystal is $T = \exp(-\alpha z)$, where $\alpha = 1/l_{at}$ is the absorption coefficient, and z the thickness of the material. This implies a transmission of 98% of the driving-pulse intensity for a 200 μm thick MgO sample.

It is important to compare the values of the optical properties of MgO and MgO:Cr. However, to the best of our knowledge, the optical constants for MgO:Cr with 5000 ppm dopant concentration are not tabulated. According to the literature on wide bandgap crystals (as Ti:Sapphire, CaF_2 or SrF_2) with low dopant concentrations¹⁸⁻²¹, we assume that for our conditions the refractive index of the pristine crystal can be used for the doped one and, therefore, that propagation effects are similar in both crystals, without affecting our analysis. Possible effects of nonlinear phenomena, such as Kerr self focusing, are currently under investigation.

SI.3. THEORETICAL MODEL FOR HHG IN SOLIDS WITH VACANCY DEFECTS

We numerically solve the Semiconductor Bloch Equations (SBEs)²²⁻²⁸

$$[\hat{H}, \hat{\rho}(t)] = i\dot{\hat{\rho}}(t), \quad (\text{S1})$$

where $\hat{\rho}(t)$ is the density operator. The Hamiltonian of the system can be written in the velocity gauge as

$$\begin{aligned} \hat{H} &= \frac{1}{2} \hat{\mathbf{p}}^2 + \mathbf{A}(t) \cdot \hat{\mathbf{p}} + V(\mathbf{r}) \\ &= \hat{H}_0 + \mathbf{A}(t) \cdot \hat{\mathbf{p}}, \end{aligned} \quad (\text{S2})$$

where $\hat{\mathbf{p}}$ is the momentum operator, $\mathbf{A}(t)$ the vector potential of the driving laser pulse, and $V(\mathbf{r})$ the lattice potential. We

approximate the lattice potential in separated Cartesian coordinates,

$$V(\mathbf{r}) = V(x) + V(y). \quad (\text{S3})$$

Throughout this supplement we use atomic units, unless indicated otherwise. The field-free Hamiltonian and its eigenstates are given by

$$\hat{H}_0 |\phi_{n\mathbf{k}}\rangle = \varepsilon_{n\mathbf{k}} |\phi_{n\mathbf{k}}\rangle. \quad (\text{S4})$$

The corresponding field-free energy eigenvalues are $\varepsilon_{n\mathbf{k}}$. n is the band index and \mathbf{k} the crystal momentum. For the potential (S3) the eigenstates separate into 1D states along the x and y coordinate,

$$|\phi_{n\mathbf{k}}\rangle = |\phi_{nk_x}\rangle |\phi_{nk_y}\rangle, \quad (\text{S5})$$

where

$$\hat{H}_{0j} |\phi_{nk_j}\rangle = \varepsilon_{nk_j} |\phi_{nk_j}\rangle, \quad j = x, y. \quad (\text{S6})$$

The projection operator $\hat{\rho}_{\mathbf{k}}(t)$ for any crystal momentum \mathbf{k} in the first Brillouin zone (BZ) can be written as

$$\hat{\rho}_{\mathbf{k}}(t) = |\psi_{\mathbf{k}}(t)\rangle \langle \psi_{\mathbf{k}}(t)|, \quad (\text{S7})$$

in terms of solutions $|\psi_{\mathbf{k}}(t)\rangle$ of the time-dependent Schrödinger equation (TDSE)

$$\hat{H} |\psi_{\mathbf{k}}(t)\rangle = i \frac{d}{dt} |\psi_{\mathbf{k}}(t)\rangle. \quad (\text{S8})$$

Assuming a spatially homogeneous driving laser field, we separate the Hamiltonian (S2),

$$\hat{H} = \hat{H}_x^{int} + \hat{H}_y^{int}, \quad (\text{S9})$$

where

$$\hat{H}_j^{int} = \hat{H}_{0j} + A_{0j}(t)r_j, \quad j = x, y, \quad (\text{S10})$$

with $r_x = x$ and $r_y = y$. Separating the projection in Cartesian coordinates,

$$\begin{aligned} \hat{\rho}_{\mathbf{k}}(t) &= \hat{\rho}_{k_x}(t) \hat{\rho}_{k_y}(t) \\ &= |\psi_{k_x}(t)\rangle \langle \psi_{k_x}(t)| |\psi_{k_y}(t)\rangle \langle \psi_{k_y}(t)|, \end{aligned} \quad (\text{S11})$$

and expanding in eigenstates of \hat{H}_{0j} ,

$$|\psi_{k_j}(t)\rangle = \sum_n B_{nk_j}(t) |\phi_{nk_j}\rangle, \quad (\text{S12})$$

we obtain from the Liouville equation

$$[\hat{H}_x^{int} + \hat{H}_y^{int}, \hat{\rho}(t)] = i \dot{\hat{\rho}}(t) \quad (\text{S13})$$

the SBEs

$$\begin{aligned} i \dot{\rho}_{k_j}^{nn'}(t) &= -i \frac{\rho_{k_j}^{nn'}(t)}{T_2} + (\varepsilon_{nk_j} - \varepsilon_{n'k_j}) \rho_{k_j}^{nn'}(t) \\ &+ A_j(t) \sum_{n''} [P_{k_j}^{n''} \rho_{k_j}^{n''n'}(t) - P_{k_j}^{n''n'} \rho_{k_j}^{nn''}(t)] \end{aligned} \quad (\text{S14})$$

for the time evolution of the density operator in eigenstate matrix representation,

$$\begin{aligned} \rho_{k_j}^{nn'}(t) &= B_{nk_j}(t) B_{n'k_j}^*(t) \\ &= \langle \phi_{nk_j} | \hat{\rho}_{k_j} | \phi_{n'k_j} \rangle. \end{aligned}$$

The diagonal elements $\rho_{k_j}^{nn'}(t)$ represent populations of bands n , and the momentum matrix elements are defined as

$$P_{k_j}^{nn'} = \langle \phi_{nk_j} | \hat{p}_j | \phi_{n'k_j} \rangle. \quad (\text{S15})$$

T_2 is a phenomenological dephasing time, introduced to account for polarization damping²⁹, which can also be derived formally by extending the formalism to include many-body interactions, coupling with phonons, and electron-electron scattering²⁹.

The laser-driven electronic current for an initial crystal momentum \mathbf{k} is

$$\mathbf{J}_{\mathbf{k}}(t) = J_{k_x}(t) \hat{\mathbf{x}} + J_{k_y}(t) \hat{\mathbf{y}}, \quad (\text{S16})$$

with Cartesian components

$$J_{k_j}(t) = - \sum_{n'} \sum_n \langle \phi_{nk_j} | \hat{p}_{k_j} | \phi_{n'k_j} \rangle \langle \phi_{n\mathbf{k}} | \hat{p}_j | \phi_{n'\mathbf{k}} \rangle - A_j(t). \quad (\text{S17})$$

The total current and its components follow as

$$\begin{aligned} \mathbf{J}(t) &= \int_{\text{BZ}} J_{\mathbf{k}}(t) d^2\mathbf{k} \\ &= \frac{2\pi}{a} \hat{\mathbf{x}} \int_{-\pi/a}^{\pi/a} J_{k_x}(t) dk_x + \frac{2\pi}{a} \hat{\mathbf{y}} \int_{-\pi/a}^{\pi/a} J_{k_y}(t) dk_y \\ &= J_x(t) \hat{\mathbf{x}} + J_y(t) \hat{\mathbf{y}}, \end{aligned} \quad (\text{S18})$$

allowing us to calculate the spectral HHG yield as

$$\begin{aligned} Y(\omega) &= \left| \int_{-\infty}^{\infty} dt e^{-i\omega t} \mathbf{J}(t) \right|^2 \equiv |\hat{\mathbf{J}}(\omega)|^2 \\ &= \left| \int_{-\infty}^{\infty} dt e^{-i\omega t} [J_x(t) \hat{\mathbf{x}} + J_y(t) \hat{\mathbf{y}}] \right|^2 \\ &\equiv |\hat{J}_x(\omega)|^2 + |\hat{J}_y(\omega)|^2. \end{aligned} \quad (\text{S19})$$

We model the MgO band structure in each spatial dimension by the cosine potential^{25,30,31}

$$V_j(x) = V_0 \cos(ar_j), \quad (\text{S20})$$

with $V_0 = 0.37$ a.u. and lattice parameter $a = 8$ a.u. Even though this potential matches adequately the bandwidth of the two lowest bands of MgO in the $\Gamma - X$ direction, it produces a minimum band gap of 4.2 eV. We therefore shift the valence band downwards³² to adjust the minimum band gap to the experimental value of 7.8 eV (Fig. S3).

We represent the MgO:Cr band structure for 0.5% Cr doping taking into account both, the substitution of Mg by Cr ions and the presence of Mg vacancies, by modifying the potential of the pristine sample³³⁻³⁷. To account for the effect of

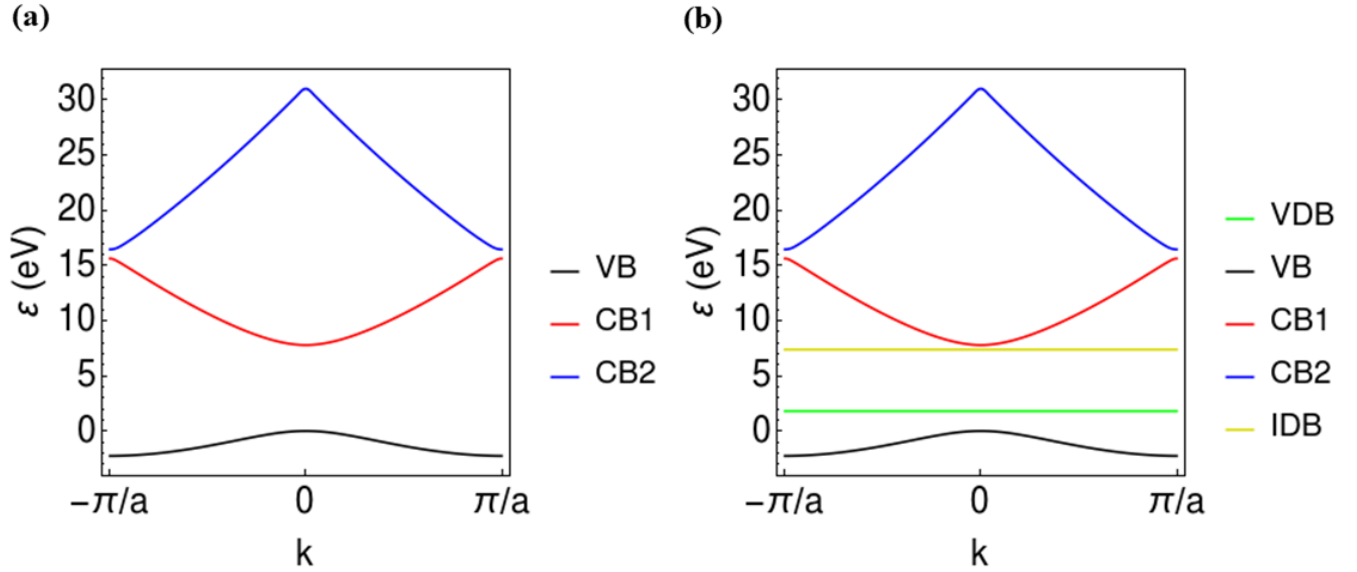


FIG. S3: Energy bands used in the calculation. Valence (VB) and two conduction bands (CB1 and CB2) of the (a) pristine MgO and (b) MgO:Cr crystal. Panel (b) includes the vacancy defect (VDB) and impurity defect (IDB) bands of MgO:Cr.

vacancies, we increase the oscillation amplitude at a position $n_{vac}a$. Furthermore, accounting for the substitution of Mg^{2+} by Cr^{3+} , we decrease the oscillation amplitude at a neighbouring lattice position $n_{imp}a$. This results in the modified electronic potential

$$V_j(x) = V_0 \cos(ar_j) + \begin{cases} V_{vac} \cos(ar_j), & n_{vac}a \leq x \leq (n_{vac} + 1)a \\ V_{imp} \cos(ar_j), & n_{imp}a \leq x \leq (n_{imp} + 1)a \end{cases}, \quad (\text{S21})$$

where V_0 , V_{vac} , and V_{imp} are the pristine solid, the impurity, and the vacancy potential strength, respectively. The 0.5% dopant concentration amounts to one Cr ion for every 200 lattice sites. We match the band gap reduction of 1.8 eV observed for MgO:Cr (Sec. SI.2) for $V_{imp}=0.11$ a.u. and $V_{vac} = -0.11$ a.u. For the low dopant concentrations used in the present work, we may approximate defect states as non-dispersive levels in the band gap with an infinite effective mass. These states couple along the entire BZ to excite conduction band levels³⁷. This coupling is allowed since the presence of impurities breaks the translational symmetry of the pristine lattice, while the pristine MgO crystal only allows optical transitions between states of equal crystal momentum within the first BZ. However, due to our low defect concentration, the electronic band structure of MgO is only slightly modified, consistent with our DFT calculations (Sec. SI.4). We therefore approximate the coupling between bands as strictly vertical. In summary, we model the band structure of MgO:Cr used in our calculation in terms of dispersive valence- and conduction-bands of the pristine crystal with two modifications: (i) an adjusted band-gap energy (Sec. SI.2.) and two added flat (i.e., non-

dispersive) bands accounting for vacancy and impurity states, as shown in Fig. S3.

Neglecting temperature effects, the Fermi level for the doped crystal lies between the valence and lowest conduction band of MgO³⁸. The valence band and vacancy state are thus occupied, while higher bands are unoccupied.

The weak yield of HH 18 from MgO:Cr is likely due to numerical noise brought into our SBE solution by the added IDB and VDB (Fig. 2). Numerically, noise can be reduced by assuming a very small dephasing time. Even though a precise experimental quantification of the dephasing time is difficult, taking extremely small dephasing has been described as unphysical²⁸. We here decided to employ a constant dephasing time T_2 , adjusted to a quarter-cycle of driving-laser optical period, following Ref.²⁵. When integrating the yield, we only include odd harmonics, in order to not over-estimate the yield from the doped sample, because, as shown Fig. 2 (b), the numerical calculation for the doped sample exhibits low-contrast spurious even harmonic contributions at high intensities, which are not observed experimentally.

We model the laser field with a 5-cycle flat-top envelope. In all calculations we employ a fourth-order Runge-Kutta algorithm to numerically solve the SBE (S14) at 400 equally spaced k -points in the first BZ.

SI.4. APPEARANCE OF VACANCY-INDUCED DEFECT STATES IN MgO:Cr FROM DENSITY FUNCTIONAL THEORY

We perform *ab initio* density functional theory (DFT) simulations of the doped MgO with $6 \times 6 \times 6$ supercells, using only the Γ point to represent the Brillouin zone. This yields a defect

concentration of 0.46%, very similar to the 5000 ppm concentration of the experimental samples. To get a reliable band-gap energy, we employ the Tran-Blaha (TB09) functional³⁹. Our simulations are performed with the Octopus code⁴⁰. We employ a grid spacing of 0.2 Bohr, norm-conserving pseudopotentials, and a lattice constant of 4.212Å. A Fermi-Dirac smearing of the electronic temperatures of 25 meV is used in all the calculations. For undoped MgO, this gives a band gap of 7.70 eV, which is quite close to the experimental value of 7.8 eV¹⁰. The Cr defect, as well as Mg vacancies, are non-magnetic defects. Spin degrees of freedom, as well as spin-orbit coupling, are neglected in the simulations. We investigate different situations: (i) undoped MgO, (ii) Cr-doped MgO with a concentration of 0.46% defect, (iii) Cr-doped MgO with the same concentration with a neighboring Mg vacancy. The structures have been relaxed using the Quantum Espresso code⁴¹ at the level of the local density approximation. Various models have been proposed in the past concerning the structure of the Mg vacancy of Cr-doped MgO⁴². Here we perform simulations for both the C_{2v} and the C_{4v} structures⁴², which correspond, respectively, to a vacancy located at the closest neighbor along the [110] or [100] direction.

Our results are presented in Fig. S4. Compared to undoped MgO, we find that Cr doping can introduce in-gap defect states, in agreement with previous work performed at the level of the local density approximation complemented within a Hubbard model and by experimental results⁴³. We find that the Cr doping alone does not alter the valence bands of MgO, and does not produce a clear in-gap defect state, except for a defect state close to the bottom of the conduction bands. However, if we also create a Mg vacancy close to the Cr atom, we observe a significant reduction of the band gap, of about 0.6 eV, due to the appearance of defect states above the topmost valence band. We find that this complex defect center, besides adding occupied defect states within the band gap of pristine MgO, also modifies the top-most valence bands of MgO. The density of states in both cases are found to be quite similar for the C_{2v} and C_{4v} structures, indicating that the change in band gap does not rely strongly on the vacancy to be at a given neighboring site close to the Cr atom. This suggests that a simplified modeling of the defect, taking into account in-gap defect states and neglecting the microscopic details of the defect, is physically acceptable.

We performed DFT calculations for a wide range of concentrations and do not find a significant dependence of the gap on the concentration. However, the defect concentration can vary locally in the experiment.

The performed DFT calculations therefore support the results obtained by the one-dimensional model presented in Sec. SI.3. In particular, they show the position of the occupied defect state close to the top of the valence band within the gap of pristine MgO.

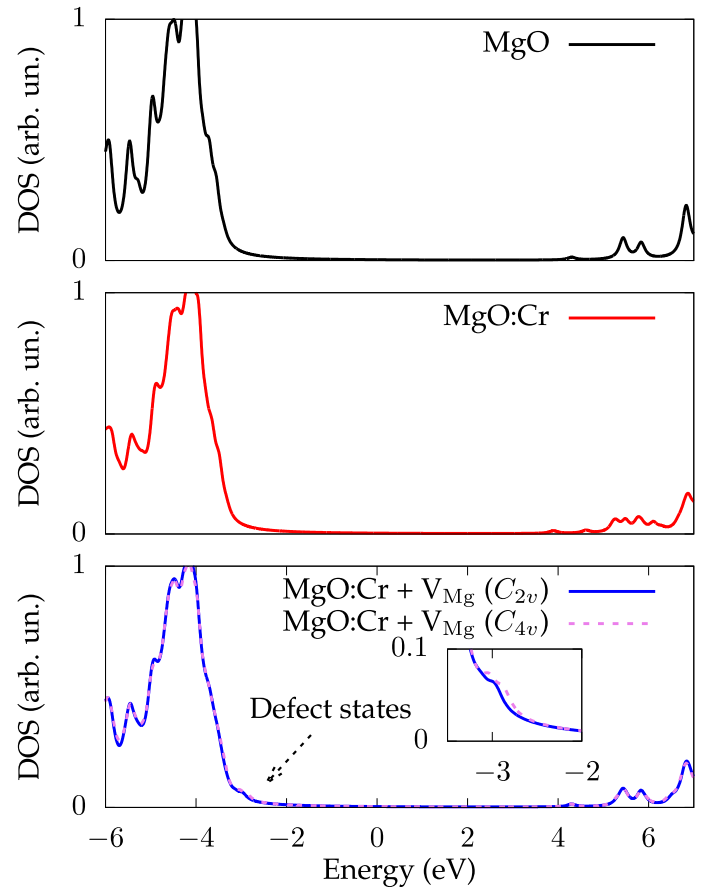


FIG. S4: Comparison of the density of states for bulk MgO (top panel), Cr-doped MgO with 5000 ppm concentration (middle panel), and Cr-doped MgO with Mg vacancies, using the C_{2v} and C_{4v} structures, as explained in the text (bottom panel).

SI.5. EXPERIMENTAL SETUP AND COMPARISON OF THE OBTAINED HHG SPECTRA

In this work, we generate harmonics in the XUV range using an intense infra-red (IR) driving field. The experiment, sketched in Fig. S5, is carried out in vacuum, at normal incidence, using a linearly-polarised laser with a wavelength centered at $\lambda_{\text{IR}} = 1.55 \mu\text{m}$ (corresponding to a photon energy of 0.80 eV), a 125 kHz repetition rate, a pulse energy on the target of up to $4 \mu\text{J}$, and a pulse duration of 22 fs full width at half maximum (FWHM). More details on the laser system are provided in Sec. SI.6. The laser beam is focused by a 5 cm focal length lens. The intensity at focus is estimated based on focal length, laser-pulse duration, calculated beam size in vacuum, and energy. The laser-intensity values provided are vacuum intensities. The maximum intensity estimated is $I=22.5 \text{ TW/cm}^2$. The laser intensity is varied by rotating the half-wave plate, and the harmonic signal is optimized by moving the samples on a motorized translation stage along the optical axis. The crystal-orientation dependence of the HHG signal is investigated by rotating the crystal on a mo-

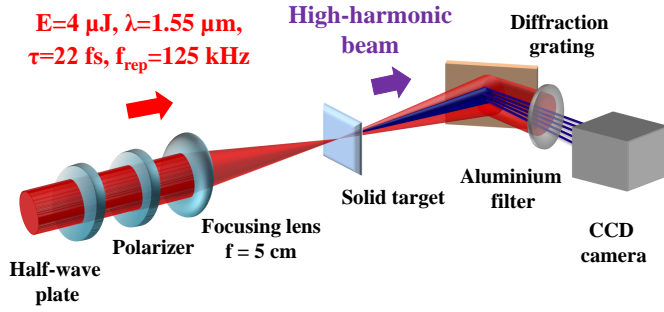


FIG. S5: (color online) Scheme of the experimental setup for HHG from MgO and MgO:Cr samples. The driving IR beam is focused into a sample producing high-order harmonics.

The emitted radiation is recorded using an XUV spectrometer, which consists of a diffraction grating and a CCD camera.

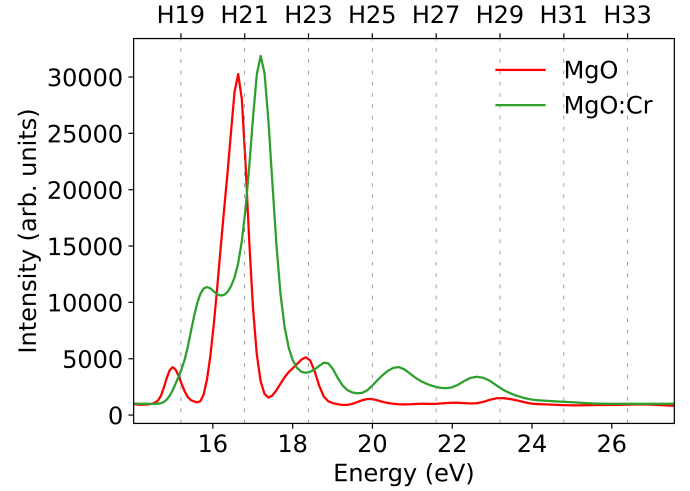


FIG. S6: Experimental HHG spectra obtained from MgO and MgO:Cr at a laser field strength of 1.05 V/\AA (14.6 TW/cm^2).

At fixed laser electric field the HHG spectra from MgO:Cr are more intense and blueshifted compared to MgO. The spectral shift is caused by the increased electron density involved in the HHG process in MgO:Cr

torized rotation stage around the laser-propagation axis.

The investigated samples, MgO and Cr-doped MgO, are $200\text{-}\mu\text{m}$ -thick with (001) oriented surfaces. For MgO:Cr, the doping concentration of Cr atoms is 5000 ppm (corresponding to $\sim 0.5\%$ defect concentration). The MgO:Cr sample was produced by the commercial company "SurfaceNet". Chromium atoms were introduced in MgO crystal during tri-arc plasma growth^{44,45}.

The interaction of the intense laser pulse with the samples results in the emission of coherent high-order harmonics, which co-propagate with the driving laser. The fundamental beam and low-order harmonics are removed by an aluminium filter allowing only XUV light to pass through it. The high-order harmonics are spectrally resolved by a home-made spectrometer composed of a reflective concave diffraction grating (McPherson 234/302, 2400 grooves/mm, Pt coated) and a back-illuminated CCD camera (Princeton Instruments, PI-MTE System; the detection exposure time was 30 seconds). The range of detected harmonics spans from order 19 (15.2 eV) to 31 (24.8 eV).

Figure S6 shows the comparison of measured HHG spectra from MgO and MgO:Cr at the laser intensity $I=14.6 \text{ TW/cm}^2$. As can be seen, there is a HHG signal enhancement as well as spectral blueshift in case of MgO:Cr compared to MgO. We associate this wavelength shift to the increased electron density participating in HHG in MgO:Cr. In the spatial domain, the electron density is higher at the center of Gaussian beam and it decreases towards the beam edges. Due to the fact that the plasma refractive index is smaller on the beam axis, its variation acts as a diverging lens. We therefore couple the observed blueshift with plasma-induced defocusing of the fundamental beam^{46–48} (and references therein).

SI.6. OPCPA LASER SYSTEM

The ultrashort pulse source at $1.55 \mu\text{m}$ relies on an optical parametric chirped pulse amplifier (OPCPA) pumped by a femtosecond ytterbium-doped fiber-based laser source at $1.03 \mu\text{m}$. This pump source delivers 400 fs, 400 μJ pulses at 125 kHz. The OPCPA is seeded by a supercontinuum generation obtained from a small fraction of the pump laser in a YAG crystal. This signal is then temporally stretched in 5 mm of silicon, and amplified in two parametric stages. The first amplification stage is based on a MgO doped periodically poled lithium niobate (MgO:PPLN) crystal and the second one on a Potassium Titanyle Arsenate (KTiOAsO₄, or KTA) crystal in non-collinear type II phase matching configuration. Compression is achieved by propagation through 210 mm of fused silica. The OPCPA output pulses are 63 fs long with an energy of 19 μJ . The pulses are then temporally compressed using soliton compression in a plate of fused silica inside a multi-pass cell. This results in the generation of 22 fs 14 μJ pulses at the cell output that are directed towards the HHG setup. The overall OPCPA architecture is described in detail in Ref.⁴⁹.

SI.7. LASER INTENSITY ESTIMATION AND NOTATION

In order to compare our experimental results with the numerical simulations, we need to be able to relate the corresponding field strengths. The intensity at the focus is estimated based on focal length, laser pulse duration, calculated beam size in vacuum, and energy. The experimental intensities are given in vacuum and do not take into account the

reflection loss on the crystal surface. Our numerical modeling relies on field strengths inside the crystals. We use the appearance of the harmonic 29 in pristine MgO as a reference for the in-vacuum field-strength value (1.23 V/Å). In this way, all field strengths used in our numerical simulations and given in the main text were corrected to in-vacuum values by multiplication with the factor 4.2.

- ¹M. O. Henry, J. P. Larkin, and G. F. Imbusch, "Nature of the broadband luminescence center in MgO:Cr³⁺," *Phys. Rev. B* **13**, 1893 (1976).
- ²A. Boyrivent, E. Duval, and R. Louat, "Broad band luminescence in MgO:Cr³⁺," *Solid State Communications* **19**, 1221 (1976).
- ³B. Henderson and G. F. Imbusch, "Optical spectroscopy of inorganic solids," Oxford University Press **23**, 2824 (1989).
- ⁴C.-C. Chao, "Charge-transfer luminescence of Cr³⁺ in magnesium oxide," *Journal of Physics and Chemistry of Solids* **32**, 2517 (1971).
- ⁵Y. Kawaguchi, "Luminescence spectra at bending fracture of single crystal MgO," *Solid State Communications* **117**, 17 (2001).
- ⁶T. Kato, G. Okada, and T. Yanagida, "Optical, scintillation and dosimeter properties of MgO transparent ceramic and single crystal," *Ceramics International* **42**, 5617 (2016).
- ⁷W. A. Sibley, C. M. Nelson, and Y. Chen, "Luminescence in MgO," *J. Chem. Phys.* **48**, 4582 (1968).
- ⁸C. Vaz, C. Moutafis, M. Buzzi, and J. Raabe, "X-ray excited optical luminescence of metal oxide single crystals," *Journal of Electron Spectroscopy and Related Phenomena* **189**, 1 (2013).
- ⁹J. Tauc, R. Grigorovici, and A. Vancu, "Optical properties and electronic structure of amorphous germanium," *Physica Status Solidi* **15**, 627 (1966).
- ¹⁰D. M. Roessler and W. C. Walker, "Electronic spectrum and ultraviolet optical properties of crystalline MgO," *Phys. Rev.* **159**, 733 (1967).
- ¹¹C. Di Valentini and G. Pacchioni, "Spectroscopic properties of doped and defective semiconducting oxides from hybrid density functional calculations," *Accounts of chemical research* **47**, 3233 (2014).
- ¹²J. Robertson and S. J. Clark, "Limits to doping in oxides," *Phys. Rev. B* **83**, 3233 (2011).
- ¹³S. Radhakrishna and B. Chowdari, "Radiation damage products in ionic crystals impurity doped alkali halides," *Fortschritte der Physik* **25**, 511 (1977).
- ¹⁴E. Vasilchenko, E. Sarmukhanov, and A. Elango, "Electronic excitations localized in NaBr and RbI crystals near vacancy defects of different sizes," *physica status solidi (b)* **185**, 189 (1994).
- ¹⁵D. Atwood, "Soft X-rays and extreme ultraviolet radiation: Principles and applications," Academic press, 63 (1999).
- ¹⁶S. Adachi, "Magnesium oxide (MgO). in: Optical constants of crystalline and amorphous semiconductors," Springer, Boston, MA, 412 (1999).
- ¹⁷E. D. Palik (editor), "Handbook of optical constants of solids," Academic press **2**, 928 (1998).
- ¹⁸A. Miller and D. Finlayson, "Laser sources and applications," CRC Press, 315 (1997).
- ¹⁹M. Lai, J. Nicholson, and W. Rudolph, "Multiple pulse operation of a femtosecond Ti:sapphire laser," *Optics communications* **142**, 45 (1997).
- ²⁰J. Philip, C. D'Amico, G. Cheriaux, A. Couairon, B. Prade, and A. Mysyrowicz, "Amplification of femtosecond laser filaments in Ti:Sapphire," *Phys. Rev. Lett.* **95**, 163901 (2005).
- ²¹Y. Guo, S. Lu, L. Su, C. Zhao, H. Zhang, and S. Wen, "Z-scan measurement of the nonlinear refractive index of Nd³⁺, Y³⁺-codoped CaF₂ and SrF₂ crystals," *Applied Optics* **54**, 953 (2015).
- ²²D. Golde, T. Meier, and S. W. Koch, "High harmonics generated in semiconductor nanostructures by the coupled dynamics of optical inter- and intraband excitations," *Phys. Rev. B* **77**, 075330 (2008).
- ²³O. Schubert, M. Hohenleutner, F. Langer, B. Urbanek, C. Lange, U. Huttner, D. Golde, T. Meier, M. Kira, S. W. Koch, and R. Huber, "Sub-cycle control of terahertz high-harmonic generation by dynamical Bloch oscillations," *Nature Photonics* **8**, 147 (2014).
- ²⁴T. Meier, G. von Plessen, P. Thomas, and S. W. Koch, "Coherent electric-field effects in semiconductors," *Phys. Rev. Lett.* **73**, 902 (1994).
- ²⁵G. Vampa, C. R. McDonald, G. Orlando, D. D. Klug, P. B. Corkum, and T. Brabec, "Theoretical analysis of high-harmonic generation in solids," *Phys. Rev. Lett.* **113**, 073901 (2014).
- ²⁶S. Jiang, H. Wei, J. Chen, C. Yu, R. Lu, and C. D. Lin, "Effect of transition dipole phase on high-order-harmonic generation in solid materials," *Phys. Rev. A* **96**, 053850 (2017).
- ²⁷J. Li, S. Fu, H. Wang, X. Zhang, B. Ding, B. Hu, and H. Du, "Limitations of the single-active-electron approximation in quantum simulations of solid high-order harmonic generation," *Phys. Rev. A* **98**, 043409 (2018).
- ²⁸I. Floss, C. Lemell, G. Wachter, V. Smejkal, S. A. Sato, X.-M. Tong, K. Yabana, and J. Burgdörfer, "Ab initio multiscale simulation of high-order harmonic generation in solids," *Phys. Rev. A* **97**, 011401 (2018).
- ²⁹H. Haug and S. Koch, *Theory of transport properties of semiconductor nanostructures* (Springer Science+Business Media Dordrecht, 1998).
- ³⁰M. Wu, S. Ghimire, D. A. Reis, K. J. Schafer, and M. B. Gaarde, "High-harmonic generation from Bloch electrons in solids," *Phys. Rev. A* **91**, 043839 (2015).
- ³¹X. Liu, X. Zhu, P. Lan, X. Zhang, D. Wang, Q. Zhang, and P. Lu, "Time-dependent population imaging for high-order-harmonic generation in solids," *Phys. Rev. A* **95**, 063419 (2017).
- ³²Y. S. You, D. Reis, and S. Ghimire, "Anisotropic high-harmonic generation in bulk crystals," *Nature Physics* **13**, 345 (2017).
- ³³T. Huang, X. Zhu, L. Li, X. Liu, P. Lan, and P. Lu, "High-order-harmonic generation of a doped semiconductor," *Phys. Rev. A* **96**, 043425 (2017).
- ³⁴C. Yu, K. K. Hansen, and L. B. Madsen, "Enhanced high-order harmonic generation in donor-doped band-gap materials," *Phys. Rev. A* **99**, 013435 (2019).
- ³⁵A. Pattanayak, M. M. S., and G. Dixit, "Influence of vacancy defects in solid high-order harmonic generation," *Phys. Rev. A* **101**, 013404 (2020).
- ³⁶H. Irvani, K. K. Hansen, and L. B. Madsen, "Effects of vacancies on high-order harmonic generation in a linear chain with band gap," *Phys. Rev. Research* **2**, 013204 (2020).
- ³⁷S. Almalki, A. M. Parks, G. Bart, P. B. Corkum, T. Brabec, and C. R. McDonald, "High harmonic generation tomography of impurities in solids: Conceptual analysis," *Phys. Rev. B* **98**, 144307 (2018).
- ³⁸C. Kittel, *Quantum Theory of Solids* (Wiley, 1987).
- ³⁹D. Waroquiers, A. Lherbier, A. Miglio, M. Stankovski, S. Poncé, M. J. T. Oliveira, M. Giantomassi, G.-M. Rignanese, and X. Gonze, "Band widths and gaps from the Tran-Blaha functional: Comparison with many-body perturbation theory," *Phys. Rev. B* **87**, 075121 (2013).
- ⁴⁰N. Tancogne-Dejean, M. J. Oliveira, X. Andrade, H. Appel, C. H. Borca, G. Le Breton, F. Buchholz, A. Castro, S. Corni, A. A. Correa, *et al.*, "Octopus, a computational framework for exploring light-driven phenomena and quantum dynamics in extended and finite systems," *The Journal of Chemical Physics* **152**, 124119 (2020).
- ⁴¹P. Giannozzi, O. Barone, P. Bonfà, D. Brunato, R. Car, I. Carnimeo, C. Cavazzoni, S. de Gironcoli, P. Delugas, F. Ferrari Ruffino, A. Ferretti, N. Marzari, I. Timrov, A. Urru, and S. Baroni, "Quantum espresso toward the exascale," *The Journal of Chemical Physics* **152**, 154105 (2020), <https://doi.org/10.1063/5.0005082>.
- ⁴²J. Aramburu, P. García-Fernández, M. Barriuso, and M. Moreno, "Transition metal complexes coupled to vacancies in oxides: Origin of different properties of Cr³⁺ in MgO bounded to a <100> or <110> Mg²⁺ vacancy," *The Journal of Physical Chemistry A* **117**, 12642 (2013).
- ⁴³M. Novita and K. Ogasawara, "Study on multiplet energies of V²⁺, Cr³⁺, and Mn⁴⁺ in MgO host crystal based on first-principles calculations with consideration of lattice relaxation," *Journal of the Physical Society of Japan* **83**, 124707 (2014).
- ⁴⁴J. Czochralski, "Ein neues Verfahren zur Messung der Kristallisationsgeschwindigkeit der Metalle," *Z. Phys. Chem.* **92**, 219 (1918).
- ⁴⁵D. Fort, "A tri-arc system for growing high-purity crystals of metallic materials," *Review of Scientific Instruments* **68**, 3504 (1997).
- ⁴⁶S. C. Rae, "Spectral blueshifting and spatial defocusing of intense laser pulses in dense gases," *Optics communications* **104**, 330 (1994).
- ⁴⁷A. Heins, S. C. Singh, and C. Guo, "Electron kinetic energy and plasma emission diagnosis from femtosecond laser produced air plasmas," *Physics of Plasmas* **24**, 072101 (2017).
- ⁴⁸V. E. Nefedova, M. F. Ciappina, O. Finke, M. Albrecht, J. Vábek, M. Kozlová, N. Suárez, E. Pisanty, M. Lewenstein, and J. Nejlid, "Determination of the spectral variation origin in high-order harmonic generation in noble gases," *Phys. Rev. A* **98**, 033414 (2018).
- ⁴⁹G. Jargot, N. Daher, L. Lavenu, X. Delen, N. Forget, M. Hanna, and P. Georges, "Self-compression in a multipass cell," *Opt. Lett.* **43**, 5643

(2018).